Supplementary material for:
Spin-polarized electronic structure of the core-shell ZnO/ZnO:Mn nanowires probed by x-ray absorption and emission spectroscopy.

A.A. Guda[1*], N. Smolentsev[1], M. Rovezzi[2], E.M. Kaidashev[3], V.E. Kaydashev[3] A.N. Kravtsova[1], V.L. Mazalova[1], A.P. Chaynikov[1], E. Weschke[4], P. Glatzel[2] and A.V. Soldatov[1]

[1] Research center for nanoscale structure of matter, Southern Federal University, Zorge 5, 344090, Rostov-on-Don, Russia
[2] European Synchrotron Radiation Facility, 6 rue Jules Horowitz, BP220, 38043 Grenoble, France
[3] Vorovich Research Institute of Mechanics and Applied Mathematics, Southern Federal University, pr. Stachki 200/1, 344090, Rostov-on-Don, Russia
[4] Helmholtz-Zentrum Berlin für Materialien und Energie, Wilhelm-Conrad-Röntgen-Campus BESSY II, Albert-Einstein-Str.15, D-12489, Berlin, Germany

1. Methods.

Details of Experiment on ID-26 beamline at ESRF. The combined energy resolution at 6539eV was 0.9eV. The optics for the incoming beam consist of three coupled undulators, a double Si(311) crystals monochromator and three Si coated mirrors working at 2.5 mrad incidence for harmonics rejection and beam focusing. The emission spectrometer runs in a vertical Rowland geometry with five Si(110) analyzer crystals working at (440) reflection, that is, around a Bragg angle of 84.2 deg. The sample is measured in horizontal grazing-incidence geometry, that is, the sample is lying on the scattering plane with an incident angle of the incoming beam of 5 degrees. The spectrometer is at 90 degrees to minimize the elastic scattering. All the samples are measured at room temperature and are tested against radiation damage. The HERFD-EXAFS spectra were collected in the total fluorescence yield mode up to a photoelectron wavenumber, k, of 12$Å^{-1}$

Calculation details. The size of the plane wave basis set and the number of K-points in the reciprocal lattice were increased until variations in the calculated spectral shape were converged. The used values were $R_{MT} \times K_{max}=7$ and 2000 k-points per ZnO unit cell (that is equal to approximately 250 k-points per 2x2x2 supercell).

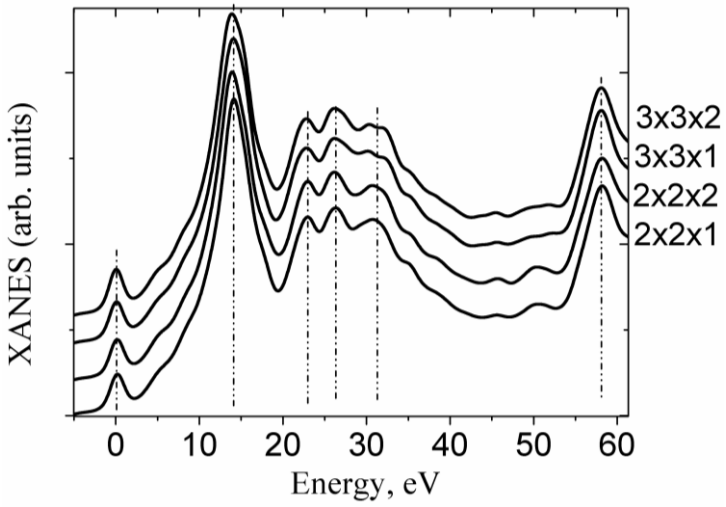

Figure S1. The effect of the supercell size on the shape of calculated Mn K-edge spectrum. Spin-restricted calculations are shown for single Mn_{Zn} defect in the supercell.

Energy convergence in the self-consistent iteration procedure was better 1meV. The generalized gradient approximation within Perdew, Burke, Ernzerhof exchange-correlation functional (GGA PBE) was used for treatment of the exchange–correlation interactions. For the ground state DOS calculations a correction for the self-interaction[1, 2] was added for localized d-electrons. U_{eff} equal 8.5eV for Zn was added in order to reproduce the experimental x-ray emission data[3]. U_{eff} for substitutional Mn_{Zn} was

calculated according to the procedure in[2] and resulted in U_{eff}=4.5eV. Spin orbit coupling was introduced via a second variational step using the scalar-relativistic eigenfunctions as basis[4]. A modified version of the exchange potential proposed by Becke and Johnson[5] was used to improve ZnO band gap, underestimated by conventional LDA.

In order to verify the effect of the theoretical approximation on the shape of the calculated spectrum we compare in Figure S2 the Mn K-edge XANES calculated for the same structures of the Mn_{Zn} in different approaches. Energy broadening for the FLAPW approximation (Wien2k software was used) is chosen same as for MTA approximation in order to fit experimental resolution (in contrast to the figure S1 where high energy resolution is applied).

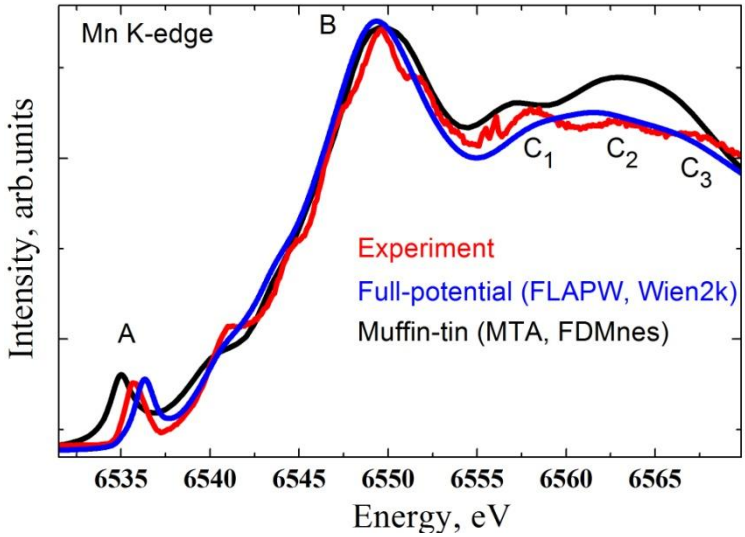

Figure S2. The effect of the chosen potential approximation. Calculations are shown for single Mn_{Zn} defect in muffin-tin approximation using FDMnes code (black) and full-potential linearized augmented plane-wave approximation using Wien2k code (blue).

Two approximations yield similar spectral shape, but with different pre-edge energy position and intensities of the peaks C_1-C_3. Green's function approach within muffin-tin approximation (FDMnes software was used[6], 9A radius for the full multiple scattering procedure, Hedin-Lundquist exchange-correlation functional) tends to overestimate the intensity of peaks C_2-C_3 while this energy region of spectra is used to identify lattice defects around Mn atoms. Thus when structural parameters are refined from the Mn K-edge XANES the muffin-tin approximation should be verified by full-potential simulations (whether it is technically possible).

2. Structure analysis.

X-ray diffraction in Figure S3 shows the high-quality of the nanowires which are free of secondary phases. However as we note in the paper standard laboratory X-ray diffraction fails to detect small amounts of dopant-related secondary phases and nanosized precipitations do not produce pronounced peaks in the diffraction pattern. For this reason, the Mn local atomic structure was investigated by Mn K-edge x-ray absorption fine structure.

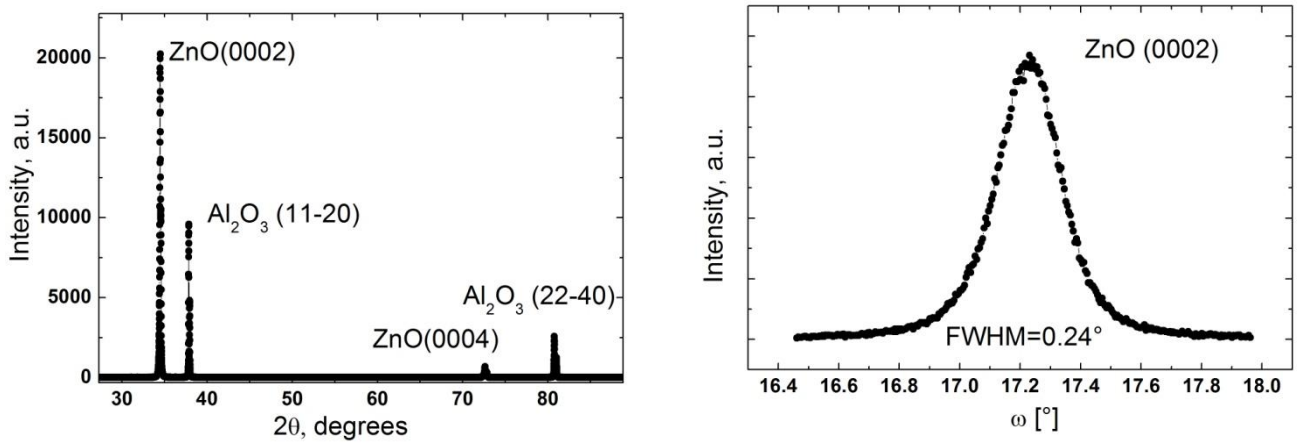

Figure S3. XRD diffractogram of a $Zn_{0.9}Mn_{0.1}O/ZnO/a\text{-}Al_2O_3$ core-shell nanowires. The rocking curve of the ZnO (0002) reflection is shown in the inset.

Figure S4 shows the comparison of the high-resolution Mn K-edge XANES of ZnO/ZnO:Mn core-shell nanowires with reference Mn oxides. Dash-dot-dot line is used for the theoretical spectrum of substitutional Mn_{Zn} defect.

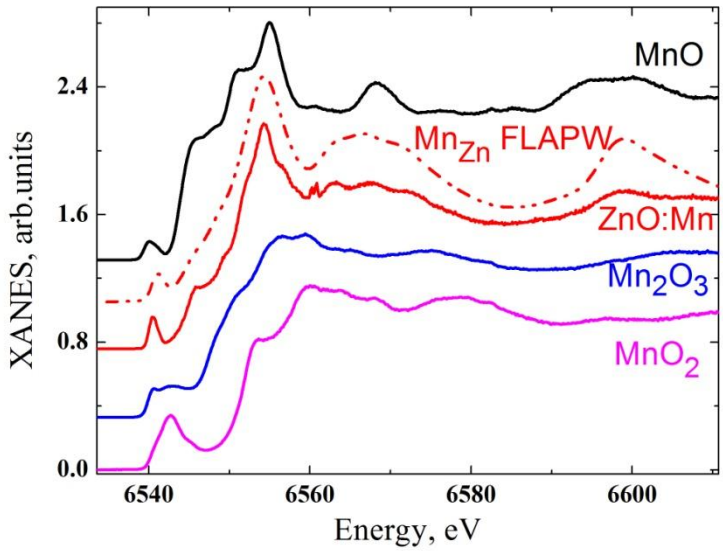

Figure S4. Mn K-edge XANES measured with high energy resolution for ZnO/ZnO:Mn core-shell nanowires and reference Mn oxides.

3. Ground state band structure of ZnO:Mn

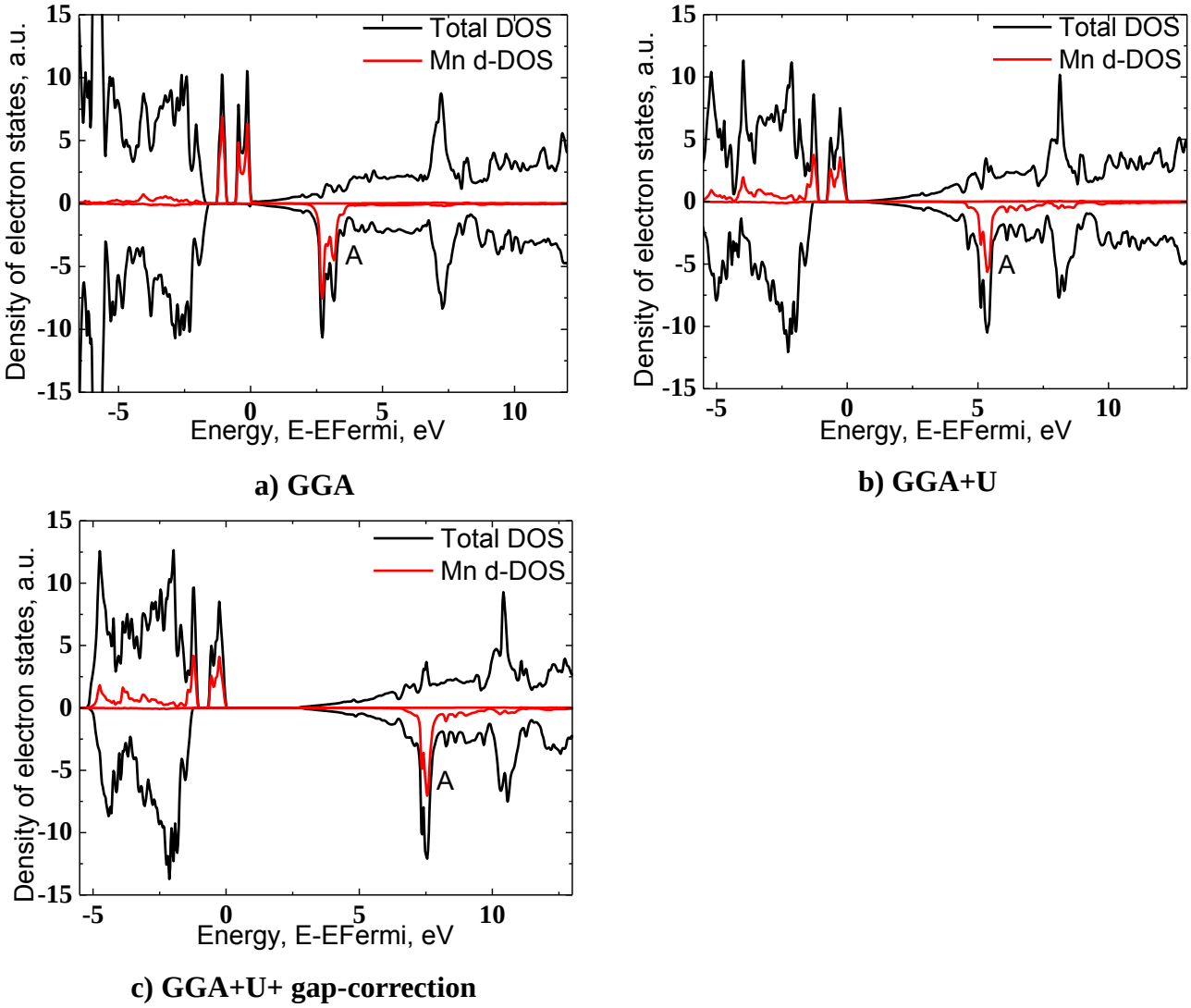

Figure S5. Calculated total and Mn d-projected electron density of states in $Zn_{0.9}Mn_{01}O$ in different approximations: a) standard GGA PBE b) GGA+U with U_{Mn}=4.5eV and U_{Zn}=8,5eV c) GGA+U with band gap correction.

The energy position of the Mn d-states strongly depends on the approximation for the exchange-correlation potential. When GGA+U is applied occupied Mn d-states are shifted to the lower energy while unoccupied are shifted to the higher energy. This follows directly from the self-interaction correction method's definition. As known DFT approximation underestimates the band gap energy. In case of ZnO:Mn the gap correction using modified version of the exchange potential proposed by Becke and Johnson[5] shifts whole valence band to the higher energies and does not move d-states relative to the band (thus such correction does not influence the relative position of peaks in XANES). In figure S6 the changes in the Mn K-edge XANES due to applied self-interaction correction are shown.

4. Mn K-edge XANES calculated within GGA+U approximation

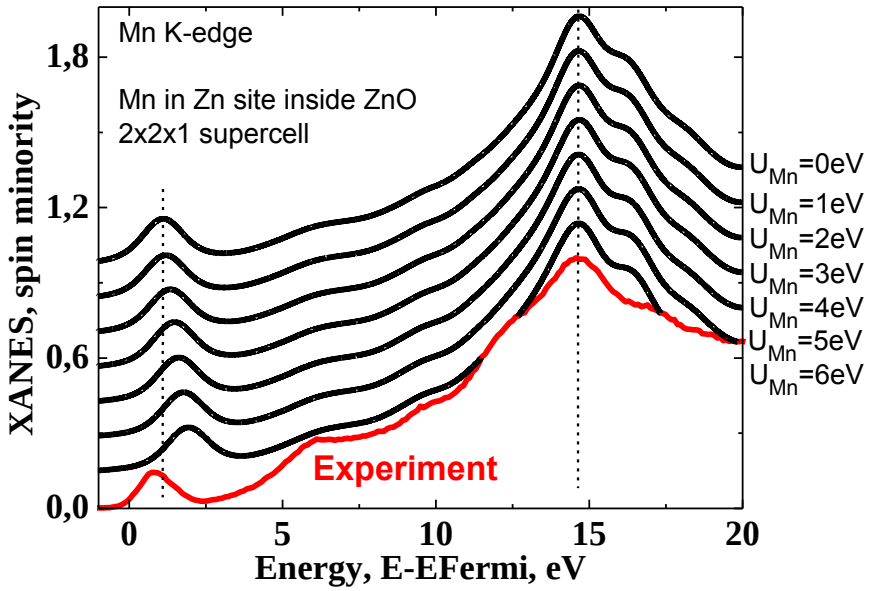

Figure S6a. Calculated spin-minority Mn K-edge in GGA+U approximation with U_{Zn}=8.5eV and U_{Mn} varying from 0eV up to 6eV. 2x2x1 supercell was used in simulations. Bottom curve is experimental Mn K-edge XANES for spin minority.

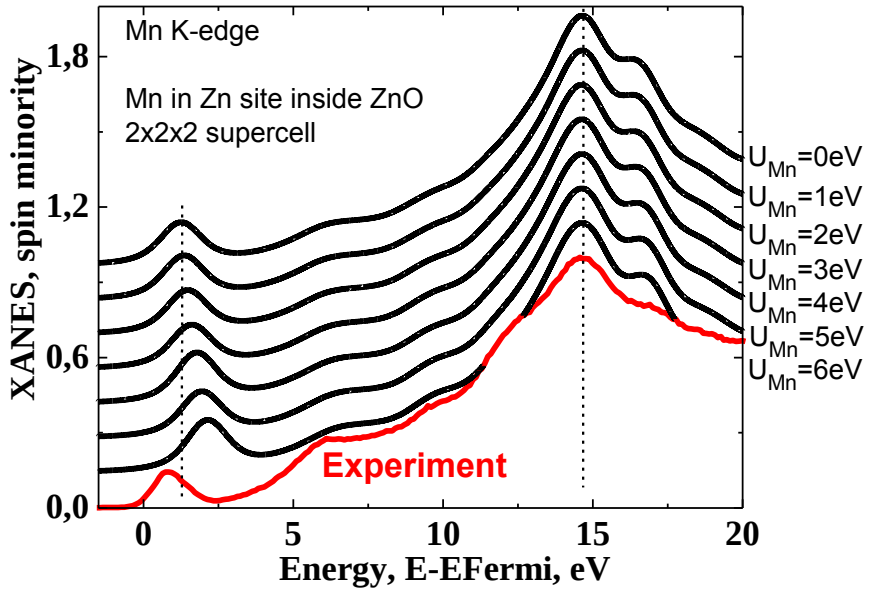

Figure S6b. Calculated spin-minority Mn K-edge in GGA+U approximation with U_{Zn}=8.5eV and U_{Mn} varying from 0eV up to 6eV. 2x2x2 supercell was used in simulations. Bottom curve is experimental Mn K-edge XANES for spin minority.

Simulation show that pre-edge peak shifts closer to the absorption maximum located near 15 eV above Fermi level. Comparison with experiment shows that a Hubbard correction does not improve the GGA results for the energy position of the unoccupied Mn d-states while this approximation is believed to be necessary for occupied TM d-states

5. Mn $L_{2,3}$ XMCD experimental data analysis.

Figure S7 (left panel) shows the circular dichroism signal in Mn $L_{2,3}$ XANES for Mn doped ZnO. Labels μ^+ and μ^- stand for the directions of the photon helicity. Positive direction of the applied magnetic field is collinear with the photon propagation direction. Sum rules for the single ion[7, 8] are used to estimate spin and orbital components to the shell-specific magnetic moment, projected onto the axis of external magnetic field:

$$m_{orb} = \frac{4}{3}\frac{\int_{L_{2,3}}(\mu_+ - \mu_-)d\varepsilon}{\int_{L_{2,3}}(\mu_+ + \mu_-)d\varepsilon}(10 - n_{3d}) = \frac{4q}{3r}(10 - n_{3d})$$

$$m_{spin} + \frac{7}{2}T_z = 2\frac{\int_{L_3}(\mu_+ - \mu_-)d\varepsilon - 2\int_{L_2}(\mu_+ - \mu_-)d\varepsilon}{\int_{L_{2,3}}(\mu_+ + \mu_-)d\varepsilon}(10 - n_{3d}) = \frac{6p - 4q}{r}(10 - n_{3d})$$

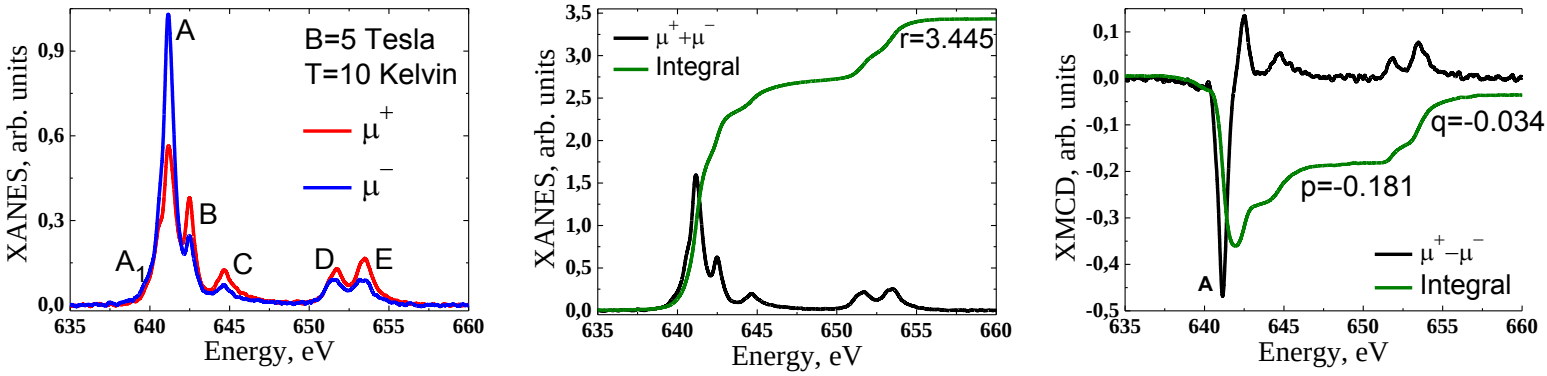

Figure S7. Mn L2,3 XANES spectra, measured for different photon helicities for ZnO:Mn, sum of polarizations and XMCD signal with corresponding integrals.

Following the procedure of data analysis described in[9] for the experimental data shown in the figure S7 we obtain m_{orb}=-0.013n_h and m_{spin}+7/2T_z=-0.276n_h in the units of Bohr magnetons. Field dependence showed the paramagnetic behaviour of sample and XMCD signal was not saturated at 5Tesla. Average value of magnetic moment projection in magnetic field B is given by the Brillouin function:

$$\langle m_z \rangle = g_{Lande}\mu_B J\left(\frac{J+1/2}{J}cth\left((J+1/2)\frac{g_{Lande}\mu_B}{k_B T}B\right) - \frac{1}{2J}cth\frac{1}{2}\frac{g_{Lande}\mu_B}{k_B T}B\right)$$

Subsequent fitting procedure of the experimental data is shown in the figure S8.

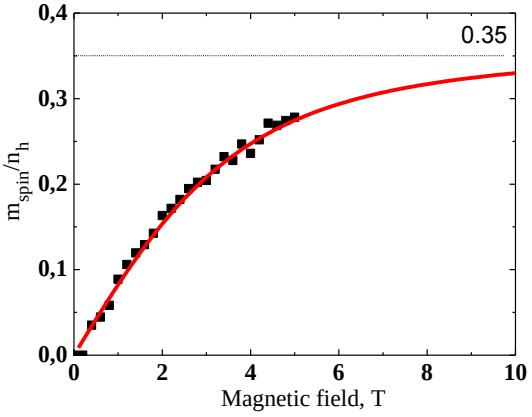

Figure S8. Field dependence of the observed Mn spin magnetic moment from the XMCD signal. Squares are the experimental data, line is a fit.

Actually, for the H parallel to the c axis implemented in the experiment, one has to use an effective spin Hamiltonian (SH) to describe field-dependent magnetization. In the case of Mn^{2+} ion a 5/2 effective spin Hamiltonian should be used. As shown in the work[10] parameters of this Hamiltonian can be obtained from electron spin resonance experiment and the SH for S = 5/2 is given by

$$\begin{aligned}\hat{\mathcal{H}}_S &= \mu_B \vec{B}\cdot\mathbf{g}\cdot\vec{S} + \vec{S}\cdot\mathbf{A}\cdot\vec{I} + D\left[S_Z^2 - \frac{35}{12}\right] + \\ &- \frac{7F}{36}\left[S_Z^4 - \frac{95}{14}S_Z^2 + \frac{81}{16}\right] + \\ &+ \frac{a}{6}\left[(S_\xi^4 + S_\eta^4 + S_\zeta^4) - \frac{707}{16}\right]\end{aligned}$$

with following eigenvalues for B || c:

$$\begin{aligned}W_{\pm 5/2} &= \pm g\mu_B B_0 - D/3 + (a-F)/2 + \\ &- \sqrt{\left[3D + \frac{a-F}{6} \mp \frac{3}{2}g\mu_B B_0\right]^2 + \frac{20}{9}a^2} \\ W_{\pm 3/2} &= \pm\frac{3}{2}g\mu_B B_0 + \frac{2}{3}D - (a-F) \\ W_{\pm 1/2} &= \mp g\mu_B B_0 - D/3 + (a-F)/2 + \\ &+ \sqrt{\left[3D + \frac{a-F}{6} \pm \frac{3}{2}g\mu_B B_0\right]^2 + \frac{20}{9}a^2}\end{aligned}$$

Paramagnetic properties are then simulated by thermally occupying the corresponding energy levels. Using D = -230×10^{-4} cm^{-1}, g = 2, and neglecting small (a-F) and a^2, we obtain the following fit function for the XMCD(μ_0H):

$$M = M_0\left[\frac{-\frac{5}{2}e^{-\frac{W_{-5/2}}{kT}} + \frac{5}{2}e^{-\frac{W_{+5/2}}{kT}} - \frac{3}{2}e^{-\frac{W_{-3/2}}{kT}} + \frac{3}{2}e^{-\frac{W_{+3/2}}{kT}} - \frac{1}{2}e^{-\frac{W_{-1/2}}{kT}} + \frac{1}{2}e^{-\frac{W_{+1/2}}{kT}}}{e^{-\frac{W_{-5/2}}{kT}} + e^{-\frac{W_{+5/2}}{kT}} + e^{-\frac{W_{-3/2}}{kT}} + e^{-\frac{W_{+3/2}}{kT}} + e^{-\frac{W_{-1/2}}{kT}} + e^{-\frac{W_{+1/2}}{kT}}}\right]$$

where T is a temperature in Kelvins. For the Mn^{2+} ion the zero field splitting is quite small (D=-$2.30\times10^{-2}$$cm^{-1}$ for Mn^{2+} while for Co^{2+} D=2.25 cm^{-1}) and this function is very close to the Brillouin function as shown in the figure S9:

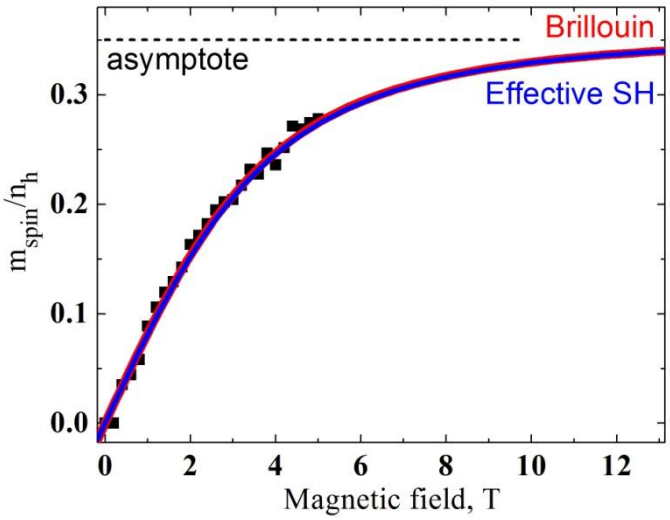

Figure S9. The fit by Brillouin function is compared to the magnetization curve obtained with spin Hamiltonian.

However if antiferromagnetic coupling is present in a sample and experimental data are obtained for high magnetic fields[11] above 10T, then Heisenberg-like term $J_{i,j}S_iS_j$ should be added to the spin Hamiltonian. This term takes into account the magnetization of coupled neighbor magnetic ions in pair, triple, quadruple etc. configurations.

The degree of polarization of the beamline should be also considered. Calculations and experimental data at the Ni edge indicate 90% - value of the Stokes parameter S3 of UE46/1-PGM-1 beamline at BESSY synchrotron. Thus final values of magnetic moments are: $\mathbf{m_{orb}=0.02n_h}$ **and** $\mathbf{m_{spin}+7/2T_z=0.39n_h}$. The dipole magnetic term is small for the Mn^{2+} ion and can be directly compared to the value of the spin magnetic moment using the two dimensional cut, shown in the Figure S10:

$$T_z = \int S_z \left(1 - 2\frac{z^2}{r^2}\right) dzdx$$

Calculations show that T_z is less than 0.1% of S_z. We can safely neglect T_z in the total three dimensional spin magnetic moment since considered plane including Mn and neighbor oxygens shows the most asymmetric cut. This is also consistent with results, obtained in[12].

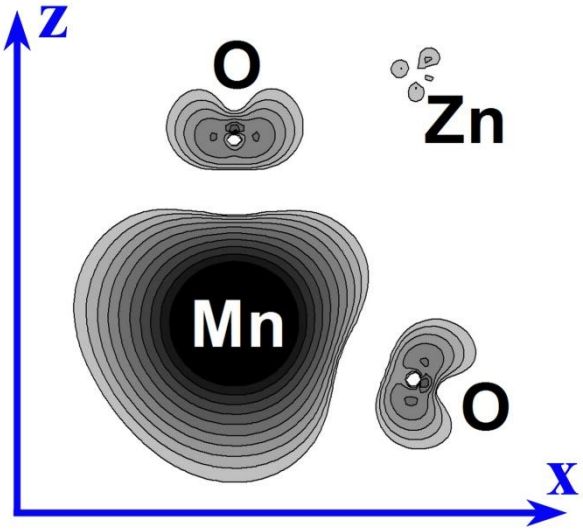

Figure S10. Spin magnetic moment distribution around Mn_{Zn} defect along $11\bar{2}0$ plane of the ZnO lattice. The logarithmic scale with 10 contour lines is used to indicate spin density values ranging from 1e/Ang^3, to 0.01 e/Ang^3.

References.

1 V. I. Anisimov, I. V. Solovyev, M. A. Korotin, M. T. Czyżyk, and G. A. Sawatzky, Physical Review B **48**, 16929 (1993).
2 G. Madsen, K. H. and P. Novák, Europhys. Lett. **69**, 777 (2005).
3 G. C. Zhou, L. Z. Sun, X. L. Zhong, X. Chen, L. Wei, and J. B. Wang, Physics Letters A **368**, 112 (2007).
4 A. H. MacDonald, W. E. Picket, and D. D. Koelling, Journal of Physics C: Solid State Physics **13**, 2675 (1980).
5 F. Tran and P. Blaha, Physical Review Letters **102**, 226401 (2009).
6 O. Bunău and Y. Joly, Journal of Physics: Condensed Matter **21**, 345501 (2009).
7 B. T. Thole, P. Carra, F. Sette, and G. van der Laan, Physical Review Letters **68**, 1943 (1992).
8 P. Carra, B. T. Thole, M. Altarelli, and X. Wang, Physical Review Letters **70**, 694 (1993).
9 C. T. Chen, Y. U. Idzerda, H. J. Lin, N. V. Smith, G. Meigs, E. Chaban, G. H. Ho, E. Pellegrin, and F. Sette, Physical Review Letters **75**, 152 (1995).
10 A. O. Ankiewicz, M. C. Carmo, N. A. Sobolev, W. Gehlhoff, E. M. Kaidashev, A. Rahm, M. Lorenz, and M. Grundmann, Journal of Applied Physics **101**, 024324 (2007).
11 A. Ney, V. Ney, F. Wilhelm, A. Rogalev, and K. Usadel, Physical Review B **85**, 245202 (2012).
12 J. P. Crocombette, B. T. Thole, and F. Jollet, Journal of Physics: Condensed Matter **8**, 4095 (1996).